

1
2 **Projections of future hydrologic drought in a reservoir-regulated region: the role of**
3 **climate change and reservoir operation**

4
5 **Shaokun He^{1,4,5}, Sirui Sun², Yanghe Liu³, Keping Chen^{1*}, Lingling Zhu¹, Yu Gong^{5*}**

6 ¹Bureau of Hydrology, Changjiang Water Resources Commission, Wuhan 430010, China.

7 ²Middle Changjiang River Bureau of Hydrology and Water Resources Survey, Bureau of
8 Hydrology of Changjiang Water Resources Commission, Wuhan 430010, China.

9 ³Three Gorges Cascade Dispatch & Communication Center, China Yangtze Power Co., Ltd.,
10 Yichang 443000, China

11 ⁴Department of Earth and Environmental Sciences, Lund University, Lund 223 62, Sweden

12 ⁵State Key Lab. of Water Resources Engineering & Management, Wuhan University, Wuhan
13 430072, China.

14

15 *Corresponding authors: chenkb@whu.edu.cn; ygong@whu.edu.cn

16

17

18 **Abstract**

19 Future hydrological droughts in reservoir-regulated regions remain unclear due to the
20 complex interactions between climate change and reservoir operation. Existing studies usually rely
21 on simplified empirical assumptions of historical reservoir operations and rarely consider the role
22 of optimal reservoir operation policies. Here, we used the upper Hanjiang River basin (UHRB) in
23 China as a case study to project its future hydrological drought evolution using standard
24 streamflow indices (i.e., SSI-1, SSI-3, and SSI-12) and to quantify the role of climate change and
25 reservoir operation. A long short-term memory (LSTM)-based hydrological model, coupled with
26 a physics-informed LSTM reservoir model, is developed and driven by bias-corrected climate
27 outputs from five global climate models to project future drought conditions under three scenarios
28 (SSP126, SSP370, and SSP585). The results indicate that future climate change over the UHRB
29 tends to reduce natural streamflow and exacerbate hydrological droughts, with the most severe
30 impacts projected in the far-future period (2071-2100) under SSP585. The traditional Ankang
31 Reservoir operation reduces the frequency, duration and severity of short-term hydrological
32 droughts (SSI-1 and SSI-3) under all scenarios, but shows limited effectiveness for long-term
33 droughts (SSI-12). Importantly, optimal reservoir operating policies that aim to maximize
34 hydropower generation and power generation guarantee rate highlight clear trade-offs between
35 hydrological drought risk and hydropower benefits, thereby underscoring the importance of
36 enhancing reservoir operation strategies for future drought management in reservoir-regulated
37 basins.

38
39 **1 Introduction**

40 Hydrological droughts, characterized by abnormally low streamflow in rivers, have
41 significant direct and indirect ramifications on hydrological, agricultural, and socio-economic

42 sectors, such as losses of crops and hydropower generation (Chang et al., 2025; Ji et al., 2023;
43 Kheyruri et al., 2023). In recent decades, hydrological droughts have become more frequent in the
44 Americas, East Asia, Africa, and Oceania, and global warming arising from high greenhouse gas
45 concentrations has been identified as the main driver (Gudmundsson et al., 2021). According to
46 the Sixth Assessment Report (AR6) of the Intergovernmental Panel on Climate Change (IPCC,
47 2021), land temperatures are projected to continue to rise, which is expected to exacerbate extreme
48 hydrological droughts in a warming future. Hence, it is of great importance to assess the
49 characteristics of extreme hydrological droughts in the context of climate change to enable
50 effective adaptation strategies.

51 At the same time, the rapid global expansion of reservoirs as a major manifestation of
52 human intervention in river systems has introduced new challenges for assessing future
53 hydrological droughts. Currently, more than 55,000 reservoirs have been registered by the
54 International Commission on Large Dams, with a total storage capacity of 14,602 km³ (Eriyagama
55 et al., 2020). Such an extensive storage capacity suggests that reservoirs can substantially affect
56 hydrological drought characteristics by regulating the spatiotemporal distribution of river flows
57 (Ho and Ehret, 2025; G. Ribeiro Neto et al., 2023). From the perspective of hydraulic regulation
58 alone, reservoirs are often found to dampen low-flow extremes in strongly regulated river basins,
59 particularly in Europe and North America, thereby alleviating drought severity during dry seasons
60 (Wanders and Wada, 2015). However, reservoirs also enable intensified consumptive water use,
61 including irrigation expansion and other anthropogenic withdrawals, which may counteract or
62 even outweigh the buffering effects of flow regulation. For example, Wan et al. (2018) reported
63 that irrigation reservoirs could increase the duration and intensity of global hydrological droughts
64 by up to 50% during 2070–2099, largely due to enhanced water abstractions. Consequently, the

65 net impact of reservoir operation on future hydrological droughts is highly region-dependent,
66 reflecting the combined effects of hydraulic regulation, reservoir-enabled water use, and the
67 heterogeneity of regional climate change.

68 Recently, some scholars have begun such drought analysis efforts in some key watersheds
69 (Sun et al., 2023; Zhang et al., 2025; Cheng et al., 2024). Yun et al. (2021b) attempted to assess
70 the effectiveness of reservoir operation in modifying hydrological extremes in the Lancang-
71 Mekong River basin using five global climate models (GCMs) from the Coupled Model
72 Intercomparison Project Phase 6 (CMIP6) and the VIC-Reservoir model. Ji et al. (2023) projected
73 hydrological drought changes in the upper Yellow River basin under different levels of global
74 warming by driving a hybrid Conjunctive Surface-Subsurface Process Version 2 (CSSPV2)
75 hydrological model coupled with a conceptual reservoir model derived from Hanasaki et al. (2006),
76 in which reservoir operations were represented using a generic rule-based formulation with
77 empirically calibrated parameters. These drought experiments demonstrated the feasibility of
78 coupling hydrological and reservoir modules for such problems, but their conclusions may remain
79 sensitive to empirical assumptions about reservoir releases when observed operating records (i.e.,
80 inflow/release/storage time series) are not explicitly used to constrain or evaluate the operating
81 representation. As one of the most influential human-engineered interventions under a changing
82 climate, reservoir systems warrant particular attention regarding the extent to which realistic
83 operating patterns can sustain system performance under plausible future scenarios (Culley et al.,
84 2016). Historical operating records contain rich decision-making information that reflects how
85 operators have adapted release strategies to diverse inflow conditions (Zheng et al., 2022).
86 Therefore, state-of-the-art tools that can systematically learn from long-term historical operating

87 records during periods with relatively stable objectives and constraints are critical for capturing
88 drought-relevant reservoir releases.

89 Against this background, machine learning (ML) offers a promising complementary
90 approach to reproducing historical reservoir operation processes. A range of data-driven ML
91 models, including artificial neural networks (ANN) (Özdoğan-Sarıkoç et al., 2023), nonlinear
92 autoregressive models with exogenous input (NARX) (Yang et al., 2019), and long short-term
93 memory (LSTM) networks (Tran et al., 2025), have been applied to simulate reservoir operations
94 using large-sample historical records. Among them, LSTM-based models have demonstrated
95 particularly favorable performance. Embedding physical mechanisms or operational constraints
96 can further enhance their ability to represent operational behaviors under hydrological extremes,
97 thereby allowing for a more accurate representation of high- and low-flow dynamics (Zheng et al.,
98 2022). Building on this line of research, coupling an LSTM-based reservoir operation module with
99 an LSTM-based hydrological process model can offer a pathway towards an integrated data-driven
100 framework for more automated drought diagnosis. This direction is motivated by key limitations
101 of traditional process-based hydrological models (e.g., VIC and CSSPV2), including their reliance
102 on basin- specific calibration and substantial requirements for physiographic inputs and
103 parameterization (e.g., topography, land use, and soil properties), which together constrain model
104 transferability across regions (Arsenault et al., 2023).

105 Beyond assessing how historical operating policies may shape future hydrological droughts,
106 it is also crucial to examine how effective optimal operating policies are in balancing operating
107 benefits against hydrological extremes. Optimal reservoir operation has been widely studied as a
108 way to enhance water-resource benefits without additional capital investment (He et al., 2025;
109 Wan et al., 2025). While some recent studies have incorporated drought-related performance

110 metrics (e.g., water-supply deficits or reliability) into operational analyses and optimization
111 frameworks (e.g., Huang et al. (2026)), these approaches primarily reflect the impacts of dry
112 conditions on water-supply performance rather than explicitly quantifying hydrological drought
113 states using drought indices. Consequently, the literature has largely focused on conceptual
114 analyses of the interplay between optimal reservoir operation and hydrological droughts, with
115 limited evidence from systematic implementation and evaluation in real-world water-management
116 practice(Huang et al., 2025; Ji et al., 2023). It therefore remains unclear whether embedding such
117 optimal strategies into existing management regimes would ultimately strengthen or weaken basin-
118 scale resilience to hydrological drought extremes under climate change.

119 Here, we aim to advance current reservoir-related drought assessment frameworks by (i)
120 replacing traditional process-based hydrological models with a fully data-driven LSTM framework
121 for hydrological drought quantification, and (ii) explicitly exploring the adaptive performance of
122 optimal operating policies under future climate change. Using the upper Hanjiang River basin in
123 China, a heavily reservoir-regulated system, as a representative case, we investigate the relative
124 and combined influences of climate change and reservoir operation on future hydrological
125 droughts under three CMIP6 shared socioeconomic pathways. Specifically, we first develop a
126 hybrid modelling framework that couples an LSTM-based hydrological model with a physics-
127 guided LSTM reservoir operation model to reproduce historical inflow and release, respectively.
128 The trained hybrid model is then driven by bias-corrected outputs from five CMIP6 GCMs to
129 project daily streamflow under near- and far-future scenarios. Hydrological drought characteristics,
130 including duration, frequency, and severity, are subsequently quantified using run theory for both
131 historical and future periods. Finally, we explicitly assess how adopting optimized operating
132 policies, in comparison with historical operating rules, may alter future hydrological drought

133 characteristics and basin-scale drought resilience, thereby revealing the potential trade-offs
134 between hydrological drought mitigation and operating benefits under a changing climate.

135

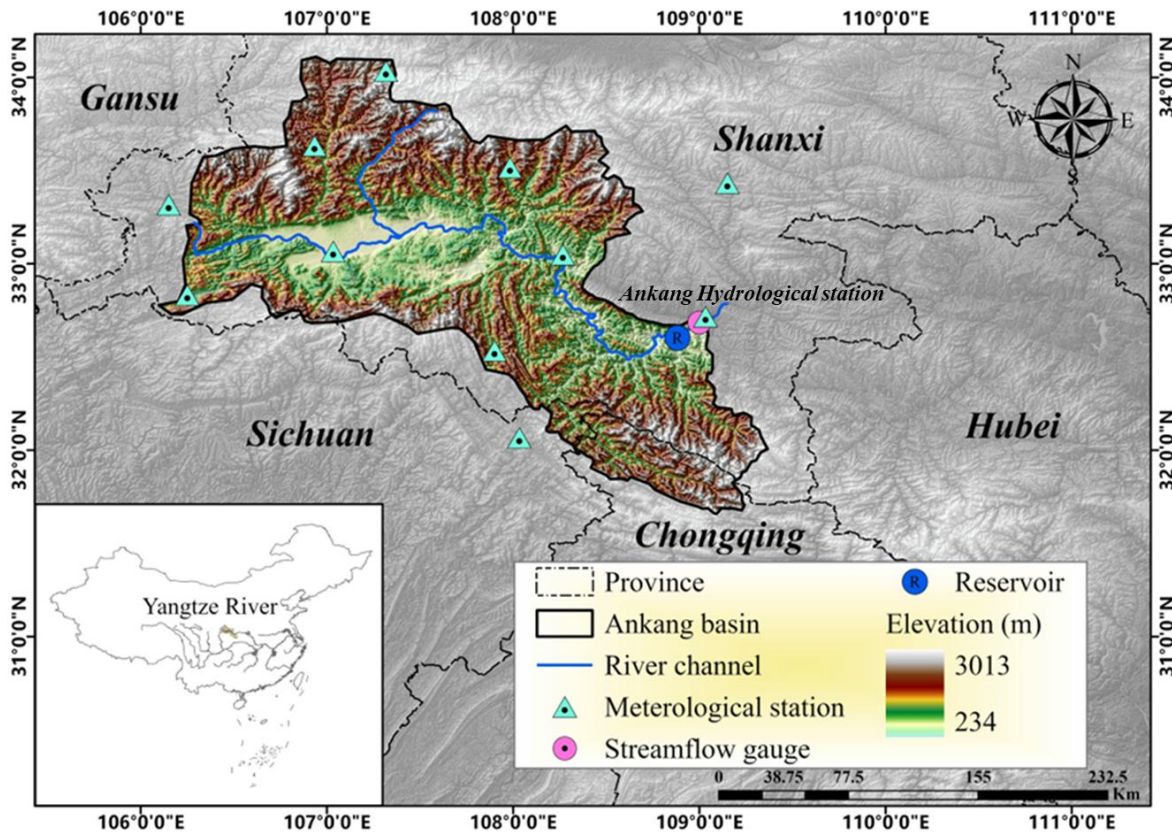
136 **2 Study Area and Data Description**

137 2.1 Study area

138 The Hanjiang River basin in central China plays a critical role in the regional water
139 economy of riparian provinces. As the longest tributary of the Yangtze River, the basin has
140 experienced extensive anthropogenic interventions, including the construction of a series of
141 reservoirs and inter-basin water transfer projects. In particular, the Ankang Reservoir, a large
142 reservoir situated near the outlet of the upper Hanjiang River basin (UHRB), exerts substantial
143 control on downstream discharge. Its operation primarily influences a ~30 km reach immediately
144 downstream (from the dam to the Ankang Hydrological Station), which we define as the regulated
145 reach in this study. As shown in Figure 1, the UHRB (31.0–34.5°N, 106.0–109.5°E) originates
146 from the southern foothills of the Qinling Mountains and terminates at the Ankang Hydrological
147 Station. The basin has a subtropical monsoon climate, with long-term mean annual precipitation,
148 temperature, and runoff depth of approximately 850mm, 15°C, and 500mm, respectively. The
149 flood season (May–October) contributes about 75% of annual precipitation, and streamflow
150 exhibits a broadly similar seasonal pattern, indicating a high sensitivity to both flood and drought
151 processes under the prevailing hydroclimatic regime (Jin et al., 2023).

152 With a total storage capacity of 3.2 billion m³, the Ankang Reservoir is the largest and most
153 downstream key control project within the UHRB. Commissioned in 1990, it is operated primarily
154 for hydropower generation (installed capacity: 850 MW), while also serving flood control and
155 navigation functions (Chinese National Committee on Large Dams, 2011). The reservoir controls

156 a natural catchment area of about 35,700 km² and has an active storage capacity of 1.47 billion m³.
157 We use discharge monitoring records collected at the reservoir upstream inlet and at the Ankang
158 Hydrological Station, which represent inflow to the reservoir and regulated releases downstream,
159 respectively.



160
161 **Figure 1.** Location of the upper Hanjiang River Basin (UHRB) and key hydrological elements,
162 showing the Ankang Reservoir and the downstream control section at the Ankang Hydrological
163 Station. The reservoir-regulated reach analysed in this study extends ~30 km downstream from the
164 dam to the station.

165
166 **2.2 Data**

167 The research datasets used in this study include both historical in-situ observations and
168 future climate projections. Historical meteorological records from eleven meteorological stations
169 (Figure 1) for the period 1992–2020 were obtained from the China Meteorological Administration

170 Data Sharing Service Center (CMA, <http://data.cma.cn>, last accessed on May 23, 2025), including
171 daily precipitation (Pr , mm), wind speed (Win , m/s), relative humidity (Rh , %), and air temperature
172 (maximum, minimum, and mean; Tem , °C). Basin-averaged precipitation and temperature time
173 series were derived using the Thiessen polygon method. Observed streamflow data for the same
174 historical period were obtained from the Bureau of Hydrology of the Yangtze Water Resources
175 Commission of China (<https://www.cjh.com.cn>, last accessed on May 23, 2025). The inflow to the
176 Ankang reservoir can be regarded as near-natural flow with negligible anthropogenic disturbance.

177 For future climate projections, a multi-model ensemble was adopted, consisting of five
178 GCMs under three Shared Socioeconomic Pathways (SSP126, SSP370, and SSP585), as listed in
179 Table 1. Several previous studies have shown that raw CMIP6 climate variables (e.g.,
180 precipitation, air temperature) tend to be overestimated in Asia, with non-negligible uncertainties
181 (Chai et al., 2022). To reduce systematic biases in climate model outputs, bias-corrected daily data
182 from the Inter-sectoral Impact Model Intercomparison Project 3b (ISIMIP3b,
183 <https://data.isimip.org/search/tree/ISIMIP3b/InputData/>, last accessed on May 23, 2025) were
184 employed. These datasets were downscaled to a spatial resolution of $0.5^\circ \times 0.5^\circ$ using
185 observational climate data and cover the period 1850–2100. In the bias-adjustment procedure, a
186 trend-preserving parametric quantile mapping method was applied, accounting for
187 interdependencies among different climate variables, thereby providing significant improvements
188 over the previous ISIMIP2 framework (Lange, 2019). The robustness of ISIMIP3b has been
189 demonstrated across many regions of China (Kang et al., 2023; Yun et al., 2021a; He et al., 2023).
190 To assess climate change impacts, three equal 30-year periods were defined: the reference period
191 (1985–2014), the near-future period (2031–2060), and the far-future period (2071–2100).

192

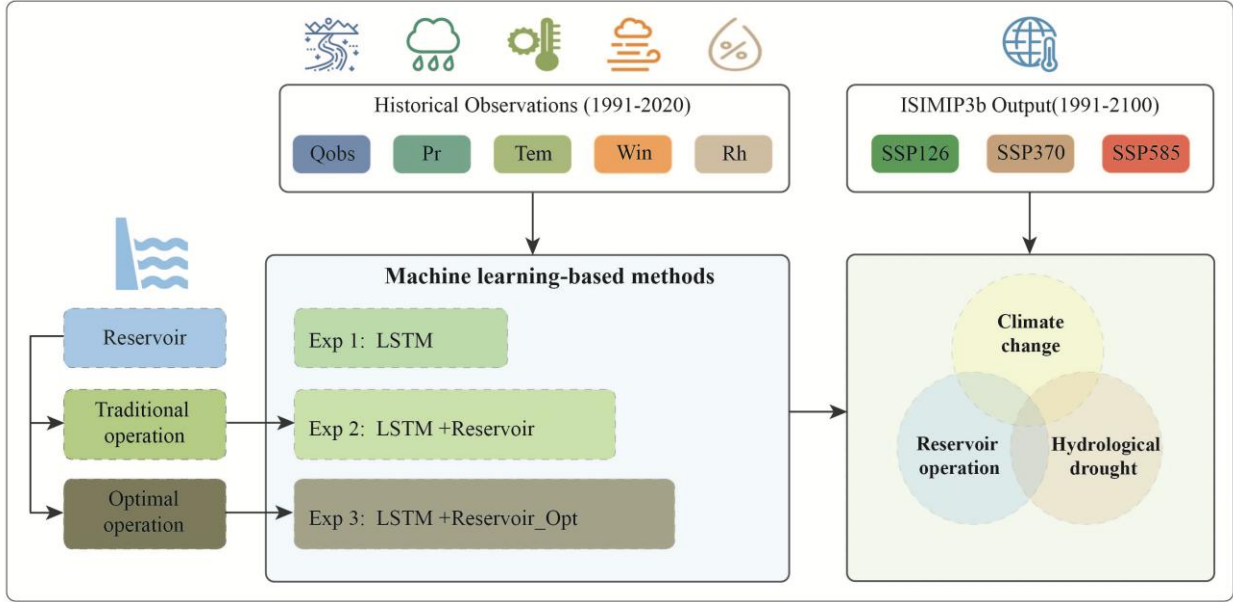
193 **Table 1.** Basic information on the five global climate models (GCMs) from ISIMIP3b

ID	Model	Modeling Center (or Group)	Institution Name	Horizontal resolution (lon. × lat.)
1	IPSL-CM6A-LR	IPSL	Institute Pierre Simon Laplace, France	$2.50^\circ \times 1.27^\circ$
2	GFDL-ESM4	NOAA-GFDL	Geophysical Fluid Dynamics Laboratory, Princeton	$1.25^\circ \times 1^\circ$
3	MPI-ESM1-2-HR	MPI-M	Max Planck Institute for Meteorology, Germany	$0.9^\circ \times 0.9^\circ$
4	MRI-ESM2-0	MRI	Meteorological Research Institute, Japan	$1.125^\circ \times 1.125^\circ$
5	UKESM1-0-LL	MOHC NERC	Met Office Hadley Centre and Natural Environment Research Council, UK	$1.25^\circ \times 1.875^\circ$

194

195 **3 Methodology**

196 This section presents the methodology for exploring future hydrological droughts under
197 the coupled effects of climate change and reservoir operation, as illustrated in Figure 2. First, an
198 LSTM-based reservoir inflow simulation and a physics-based LSTM simulation for reservoir
199 operation are performed. Then, the ISIMIP3b outputs are used to drive the hybrid modeling
200 framework to project future streamflow scenarios and identify hydrological drought
201 characteristics. Finally, a series of numerical experiments are designed to investigate the individual
202 roles of climate change and reservoir operation in shaping future hydrological droughts. Each
203 module is described in detail in the following subsections.



204

205 **Figure 2.** Schematic diagram of the modeling framework used to investigate the roles of climate
 206 change and reservoir operation in future hydrological droughts. The acronyms used in the
 207 experimental description panel are explained in Section 3.3.

208

209 3.1 Long short-term memory (LSTM)

210

211

212

213

214

215

216

217

218

219

The LSTM is a variant of recurrent neural network that uses the backpropagation-through-time algorithm to address the vanishing gradient problem and retain information from earlier time steps (Hochreiter and Schmidhuber, 1997). It is specially structured with a gated memory block that introduces a memory cell and gating mechanisms compared with conventional neural networks (Hochreiter, 1998; He et al., 2022; Chen and Yu, 2025). The memory block (shown in Figure 3a) consists of a forget gate, an input gate, an output gate, and a memory cell. The forget gate determines which information from the previous cell state is discarded, whereas the input gate determines which information is used to update the cell state. The output gate then generates the hidden state based on the updated cell state. Mathematically, a typical memory block in an LSTM can be described by Equations (1) to (5).

220

$$f_t = \sigma(x_t W_f + h_{t-1} U_f + b_f) \quad (1)$$

221

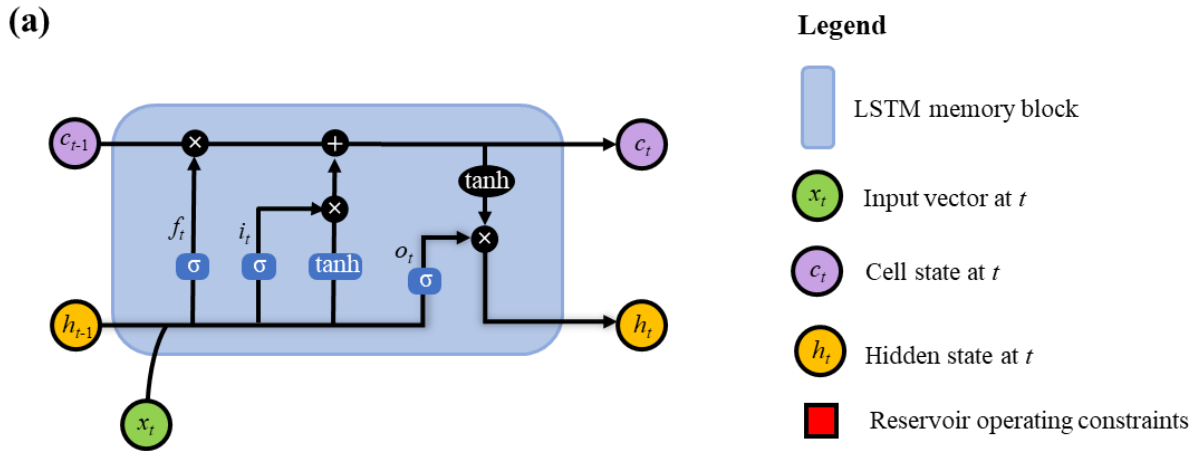
$$i_t = \sigma(x_t W_i + h_{t-1} U_i + b_i) \quad (2)$$

222
$$o_t = \sigma(x_t W_o + h_{t-1} U_o + b_o) \tag{3}$$

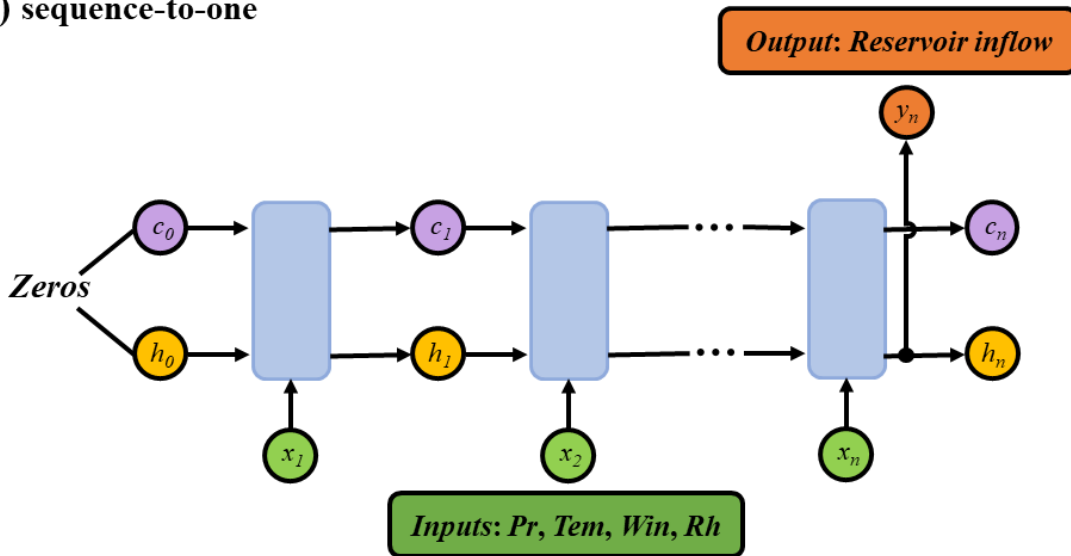
223
$$c_t = f_t \otimes c_{t-1} + i_t \otimes \tanh(x_t W_c + h_{t-1} U_c + b_c) \tag{4}$$

224
$$h_t = o_t \otimes \tanh(c_t) \tag{5}$$

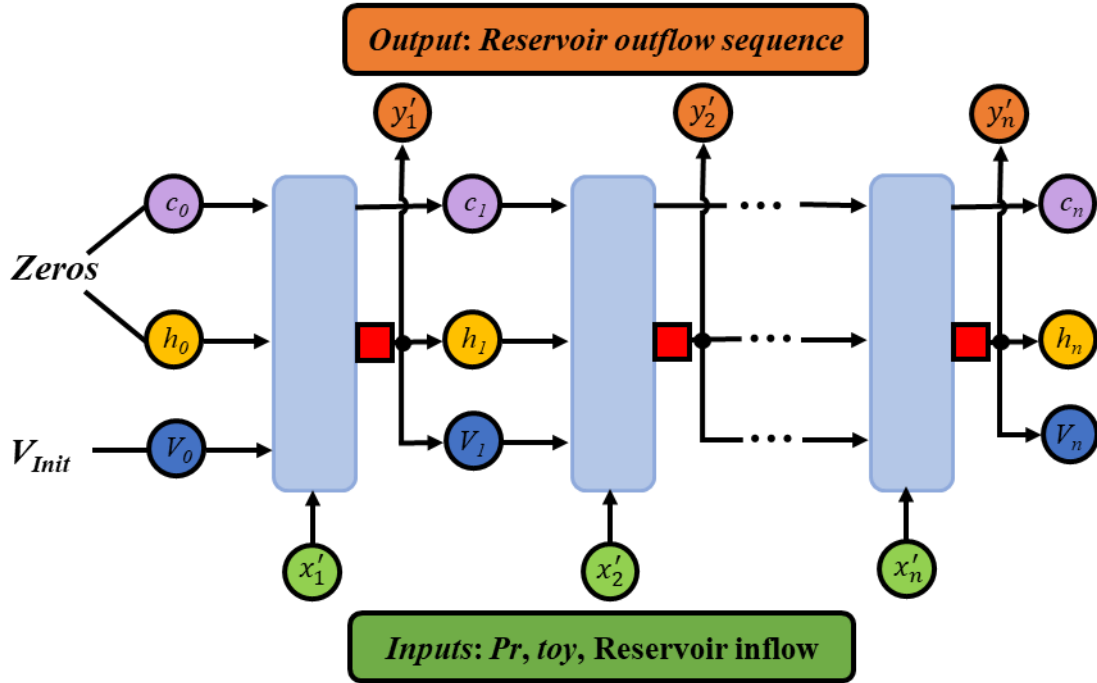
225 where x_t, f_t, i_t , and o_t denote the input variables, forget gate, input gate, and output gate at time t ,
 226 respectively. c_t and h_t represent the cell state and the hidden state at time t , while c_{t-1} and h_{t-1}
 227 are their values at the previous time $t-1$. W, U and b with various subscripts denote input weights,
 228 recurrent weights and bias terms, respectively. $\sigma(\cdot)$ is the sigmoid activation function with a return
 229 value ranging from 0 to 1. $\tanh(\cdot)$ is the hyperbolic tangent activation function with a return value
 230 ranging from -1 to 1. \otimes denotes element-wise multiplication.



(b) sequence-to-one



(c) sequence-to-sequence



231 **Figure 3.** Model structure of the long short-term memory (LSTM). (a) Internal structure of a
232 standard LSTM memory block, consisting of a forget gate, an input gate, an output gate, and a
233 memory cell. (b) A three-layer sequence-to-one LSTM architecture driven by correlated
234 meteorological inputs to simulate reservoir inflow. (c) A physics-guided LSTM-based sequence-
235 to-sequence model with antecedent reservoir storage, time of year (*toy*), precipitation and
236 simulated reservoir inflow as inputs to simulate reservoir release, where a red block following the
237 LSTM block represents a set of operational constraints, including the water balance equation and
238 reservoir storage and release limits.

239

240 3.1.1 LSTM-based reservoir inflow simulation

241 Some previous studies have shown that a three-layered LSTM with one hidden layer is
242 sufficiently robust to capture nonlinear rainfall-runoff relationships, although the black-box nature
243 of such models makes the interpretation of physical processes more challenging (Solanki et al.,
244 2025; Rehana and Rajesh, 2023; Liu et al., 2022). Following these studies, a sequence-to-one
245 LSTM architecture is adopted in this study to simulate near-natural reservoir inflow (Figure 3b).
246 The inputs to the LSTM consist of multiple meteorological variables, including precipitation, daily
247 maximum and minimum air temperature, relative humidity, and wind speed, with selected lag

248 times. The lag structure for each input variable is determined using cross-correlation analysis (Cui
249 et al., 2022) to account for delayed hydrological responses and catchment memory effects. The
250 model output is the near-natural reservoir inflow at time t . In addition to input selection, the number
251 of hidden units and the initial learning rate are treated as key hyperparameters of the LSTM model.
252 The hyperparameter tuning procedure is provided in Table S1 and was implemented using
253 TensorFlow's Keras API (Abadi et al., 2016).

254 Notably, antecedent reservoir inflow is not included as an input variable in the LSTM model,
255 although it is closely related to the target output in reality. This design choice is motivated by the
256 difficulty of accurately predicting antecedent inflow under future climate scenarios, where such
257 information can only be inferred from model simulations. Including antecedent inflow as an input
258 may therefore introduce additional uncertainty and lead to an artificial accumulation of simulation
259 errors. For historical simulations, meteorological data from 1992 to 2020 were used. The year 1992
260 was reserved as the model spin-up period to minimize the influence of initial conditions, while the
261 remaining data were divided into a calibration period (1993–2014) and a validation period (2015–
262 2020). Mean hydroclimatic conditions during the validation period were broadly comparable to
263 those during the calibration period, with no pronounced wet or dry anomaly (He et al., 2023). Thus,
264 the chronological split primarily evaluates temporal out-of-sample performance under similar
265 historical conditions rather than transferability across contrasting regimes. Model calibration was
266 performed by maximizing the Nash–Sutcliffe efficiency (NSE ; see Section 3.1.3 and Equations
267 (9)–(10)) using the Adam optimizer (Kingma and Ba, 2014). For future projections, the period
268 1985–2100 was used to cover the full simulation span of the SSP scenarios. Within this range, the
269 period 1985–2014 was designated as the reference period, following ISIMIP3b protocol, to
270 evaluate future streamflow variations against a consistent historical baseline. The calibration and

271 validation periods are used exclusively for model training and evaluation, whereas the reference
272 period is treated independently for climate impact assessment.

273 3.1.2 Derivation of historical operation patterns with a physics-guided LSTM model

274 For human-intervened reservoir operation, which often involves substantial expert knowledge,
275 LSTM, as a state-of-the-art machine learning technique, has been shown to outperform traditional
276 empirical approaches in learning operating rules from large historical records (Zheng et al., 2022;
277 Longyang and Zeng, 2023; García-Feal et al., 2022). In contrast to the inflow simulation in Figure
278 3(b), we constructed a three-layer sequence-to-sequence LSTM model (Figure 3(c)) to simulate
279 reservoir release.

280 Following the guidelines of the local reservoir management agency, antecedent reservoir
281 storage, time of year, precipitation, and reservoir inflow were used as the major inputs. To improve
282 the robustness of the model for future simulations, we used the LSTM-simulated inflow from
283 Section 3.1.1 rather than observed inflow records. In addition, a state variable representing
284 reservoir storage was incorporated and initialized at the flood-limited water level, which can be
285 updated via the state transition equation (i.e., the water balance equation in Equation (6)). To avoid
286 physically unrealistic states during the simulation (e.g., violation of operational constraints),
287 additional operational constraints, including reservoir storage limits in Equation (7) and reservoir
288 release limits in Equation (8), were also incorporated, resulting in a physics-guided LSTM model.

$$289 \quad V_{t+1} = V_t + (I_t - O_t) \cdot \Delta t \quad (6)$$

$$290 \quad V_{min} \leq V_t \leq V_{max} \quad (7)$$

$$291 \quad O_{min} \leq O_t \leq O_{max} \quad (8)$$

292 where V_t and V_{t+1} are the reservoir storage (m^3) at the beginning and end of time step t ,
293 respectively; I_t and O_t are the reservoir inflow (m^3/s) and release (m^3/s) at time t , respectively;
294 V_{min} and V_{max} are the allowable minimum and maximum reservoir storage (m^3), respectively;

295 O_{min} and O_{max} are the allowable minimum and maximum reservoir release (m^3/s), respectively;
 296 and Δt is the simulation time step (s).

297
 298 3.1.3 Objective function for model calibration

299 To simultaneously improve the simulations of near-natural reservoir inflow and human-
 300 regulated release, the average NSE (NSE_{ave}) was defined as the optimization objective.

301
$$max NSE_{ave} = 1/2 \times (NSE_{inflow} + NSE_{release}) \quad (9)$$

302 where NSE_{inflow} and $NSE_{release}$ denote the NSE values for the simulated inflow and release,
 303 respectively. For a given time series, NSE is computed as

304
$$NSE = 1 - \sum_{t=1}^T (Q_t^{sim} - Q_t^{obs})^2 / \sum_{t=1}^T (Q_t^{obs} - \overline{Q^{obs}})^2 \quad (10)$$

305 where Q_t^{sim} and Q_t^{obs} denote the simulated and observed streamflow at time t , respectively; $\overline{Q^{obs}}$
 306 is the mean observed streamflow over the evaluation period; and T is the total number of time
 307 steps. NSE ranges from $-\infty$ to 1, with 1 indicating a perfect match between simulated and observed
 308 streamflow. Although NSE tends to emphasize errors during high-flow periods because of its
 309 squared-error formulation, it was used here to calibrate overall inflow and release dynamics across
 310 the full flow regime. This choice supports the subsequent assessment of hydropower generation,
 311 and the power generation guarantee rate (Section 3.3). Hydrological drought conditions were
 312 evaluated separately using SSI and run-theory-based duration and severity metrics, and the
 313 remaining sensitivity to NSE -based calibration is discussed in Section 4.5.

314 3.2 Standardized streamflow index

315 This study used the standardized streamflow index (SSI) to characterize hydrological
 316 drought, because it only requires streamflow data and has been widely applied across a range of
 317 timescales, including 1-, 3-, 12-, and 24-month periods (Vicente-Serrano et al., 2012; Smith et al.,
 318 2019; Gu et al., 2020; Shukla and Wood, 2008). The 1-month (SSI-1) and 3-month (SSI-3) indices

319 represent short-term hydrological conditions, whereas longer aggregation windows such as SSI-
 320 12 and SSI-24 reflect persistent, long-term hydrological drought conditions. Here, SSI-1, SSI-3,
 321 and SSI-12 were selected to represent monthly, seasonal, and annual hydrological drought,
 322 respectively.

323 In the calculation of SSI for each calendar month m ($m = 1, 2, \dots, 12$) at a specific time
 324 scale, a Pearson type-III distribution was fitted to the corresponding aggregated streamflow series
 325 (Q) during the reference period. The goodness-of-fit was evaluated using the Kolmogorov–
 326 Smirnov test. The cumulative distribution function is expressed as:

$$327 \quad F_m(Q) = \frac{\beta^\alpha}{\Gamma(\alpha)} \int_x^\infty (Q - \omega)^{\alpha-1} e^{-\beta(Q-\omega)} dr \quad (11)$$

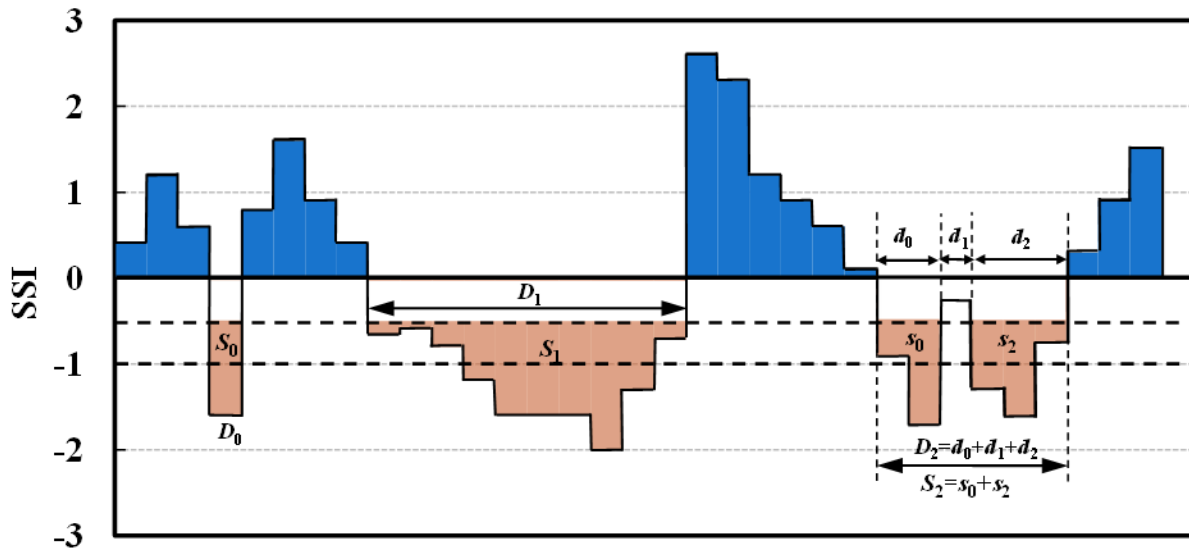
328 where $F_m(Q)$ is the cumulative distribution function; α , β , and ω are the shape, scale, and location
 329 parameters of the distribution, respectively, which were estimated using the L -moment method
 330 (Hosking, 1990). The SSI values were then obtained by applying the standard normal transforming
 331 process (Φ^{-1}).

$$332 \quad SSI = \Phi^{-1}(F_m) \quad (12)$$

333 To ensure consistency in comparing hydrological drought characteristics between
 334 historical and future periods, the distribution parameters estimated from the 30-year reference
 335 period (1985–2014) were applied to the two future 30-year periods (i.e., the near-future and far-
 336 future) when computing SSI, following common practice in climate impact assessment studies
 337 (Yun et al., 2021b; Wan et al., 2018).

338 The characteristics (e.g., duration, severity, and intensity) of hydrological drought episodes
 339 were extracted using run theory (Yevjevich, 1967). A drought episode begins when SSI falls below
 340 a specific threshold (-0.5) and ends when SSI rises above the threshold, as illustrated by the two
 341 drought episodes D_0 and D_1 in Figure 4. Drought duration is defined as the length of the drought

342 episode, while drought severity is defined as the cumulative deficit of SSI values below the drought
 343 threshold during the episode. Drought intensity is defined as the average deficit below the
 344 threshold, calculated as severity divided by duration. In particular, two adjacent drought branches
 345 (d_0 and d_2) can be merged into a single drought episode (i.e., the third drought episode in Figure
 346 4) when the inter-event time d_1 is no longer than the time evaluation criterion t_c ($t_c = 2$ months in
 347 this study) and SSI remains below the allowable upper threshold during this interval (Zhou et al.,
 348 2021; Wu et al., 2017). Under this condition, the merged drought duration is calculated as $D_2 = d_0$
 349 $+ d_1 + d_2$ and the severity is $S_2 = s_0 + s_2$. Since drought intensity is defined as the ratio of severity to
 350 duration, only two drought characteristics, duration (D) and severity (S), are used in this study to
 351 comprehensively describe each drought episode.



352
 353 **Figure 4.** Identification of hydrological drought events and characteristics using run theory. Three
 354 types of drought episodes are illustrated in orange: episode D_0 with severity S_0 , episode D_1 with
 355 severity S_1 , and a merged episode D_2 with severity S_2 , where $D_2 = d_0 + d_1 + d_2$ and $S_2 = s_0 + s_2$. The
 356 two adjacent drought branches d_0 and d_2 are merged when the interval d_1 is no longer than the time
 357 evaluation criterion t_c ($t_c = 2$ months in this study) and the SSI remains below the allowable upper
 358 threshold during d_1 .

359

360 3.3 Experimental Design

361 To systematically explore the roles of climate change and reservoir operation in shaping
362 future hydrological droughts, a set of numerical experiments was designed (Table 2). Specifically,
363 OBS/LSTM and OBS/LSTM+Reservoir denote simulations driven by observed CMA
364 meteorological forcing, without and with reservoir operation, respectively. Similarly,
365 ISIMIP3b_ref/LSTM and ISIMIP3b_ref/LSTM+Reservoir represent simulations driven by
366 ISIMIP3b forcing during the reference period, without and with reservoir operation, respectively.
367 The experiments ISIMIP3b_fut/LSTM and ISIMIP3b_fut/LSTM+Reservoir further incorporate
368 future climate forcing to quantify the progressive impacts of climate change and reservoir
369 operation on future projections. Notably, the term “Reservoir” in these experiments refers to the
370 historical reservoir operation policy over 1992–2020, which was derived from the physics-guided
371 LSTM model.

372 Little attention has been paid to the evolution of trade-offs between operating benefits and
373 drought risks, although a large body of literature points out the necessity of optimizing reservoir
374 operation policies (Ji et al., 2023; Brunner, 2021; Wu et al., 2022; Firoz et al., 2018). To this end,
375 a classical multi-objective decision-making optimization was implemented for the Ankang
376 Reservoir to maximize both hydropower generation and the power generation guarantee rate. The
377 optimal set of alternative operating policies π_θ^* under historical climate conditions w^H was
378 obtained by solving the following problem.

$$379 \quad \pi_\theta^* = \underset{\pi_\theta}{\operatorname{arg\,max}} f(\pi_\theta, w^H) = |f_{THP}(\pi_\theta, w^H), f_{PGR}(\pi_\theta, w^H)| \quad (13)$$

380 where f is the objective vector consisting of $[f_{THP}, f_{PGR}]$ (see Text S2 for details). The operating
381 policies π_θ was parameterized using Gaussian radial basis functions, which have been shown to
382 be effective for reservoir operation optimization (Quinn et al., 2019; Bertoni et al., 2019). The

383 optimization was performed using the Non-dominated Sorting Genetic Algorithm II (NSGA-II;
384 (Deb et al., 2002). The resulting Pareto-optimal policies, π_{θ}^* , were then applied under future
385 climate scenarios to investigate the potential co-benefits and trade-offs between hydropower
386 generation and drought risk reduction. This exploratory analysis corresponds to the
387 ISIMIP3b_fut/LSTM+Reservoir_Opt experiment in Table 2, and detailed results are presented in
388 Section 4.4.

389 **Table 2.** Experimental design and scenario configurations used in this study.

Experiment	Meteorological forcing	Simulation period	Climate change	Traditional reservoir operation	Optimal reservoir operation
OBS/LSTM	Observations	1992–2020	–	–	–
OBS/LSTM + Reservoir	Observations	1992–2020	–	✓	–
ISIMIP3b_ref/LSTM	ISIMIP3b reference	1985–2014	–	–	–
ISIMIP3b_ref/LSTM+Reservoir	ISIMIP3b reference	1985–2014	–	✓	–
ISIMIP3b_fut/LSTM	ISIMIP3b future	2031–2060, 2071–2100	✓	–	–
ISIMIP3b_fut/LSTM+Reservoir	ISIMIP3b future	2031–2060, 2071–2100	✓	✓	–
ISIMIP3b_fut/LSTM+Reservoir_Opt	ISIMIP3b future	2031–2060, 2071–2100	✓	–	✓

390

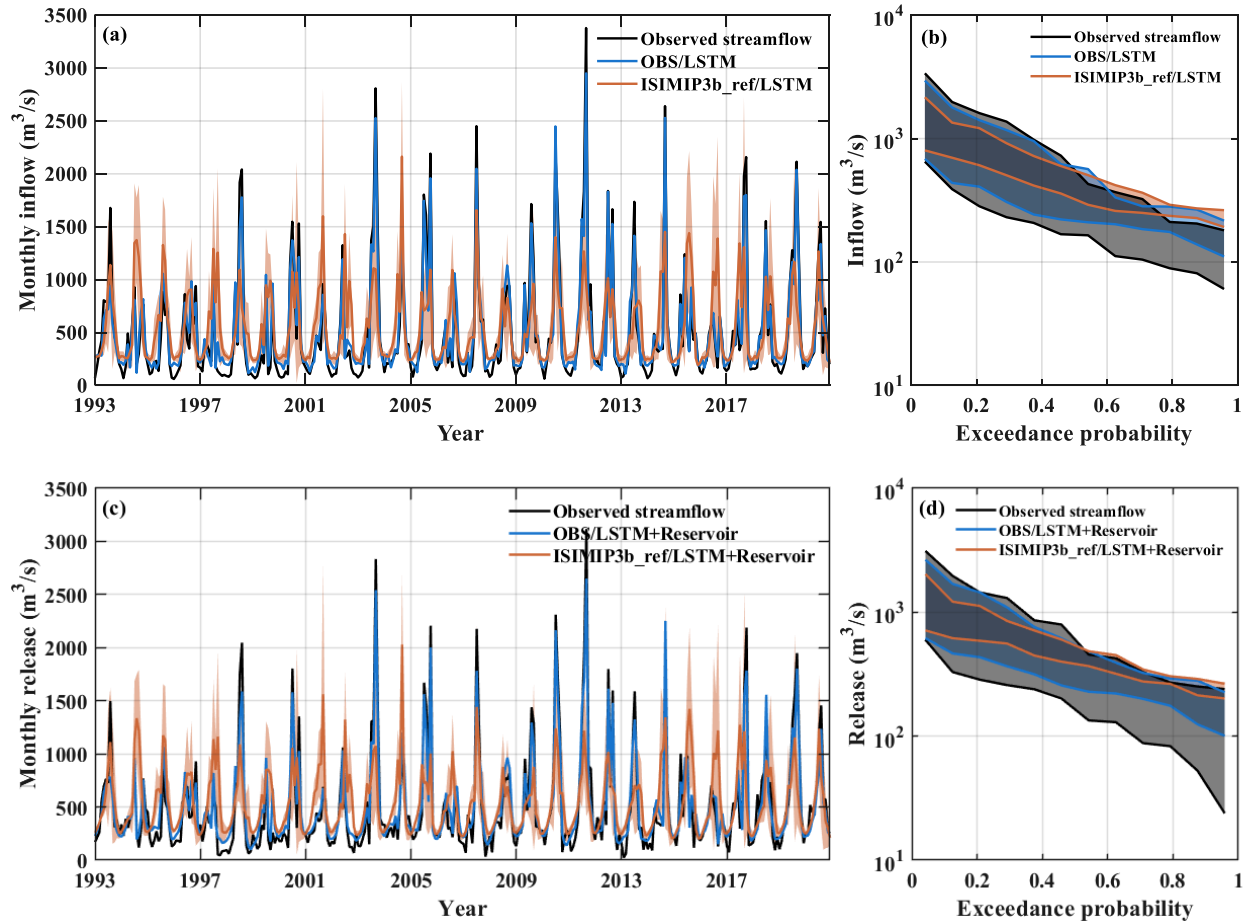
391 **4 Results and Discussion**

392 4.1 Model calibration and validation

393 Figure 5 presents the calibration and validation results for both reservoir inflow and release
394 using the LSTM-based modeling framework. As shown in Figure 5(a), the LSTM model
395 reproduced the near-natural reservoir inflow well at the monthly scale, with *NSE* values of 0.95
396 and 0.93 for the calibration and validation periods, respectively. Figure 5(b) further evaluates the

397 model performance across the full flow regime using flow duration curves (FDCs), showing that
398 the simulated flow distribution generally follows the observed pattern across a wide range of
399 exceedance probabilities. Figure 5(c) illustrates the comparison between observed and simulated
400 reservoir release at the Ankang hydrological station. The seasonal shift between observed inflow
401 and release curves (black lines in Figure 5(a) and 5(c)) suggests that reservoir operations have
402 reshaped streamflow seasonality, with an estimated 5–21% of downstream flow withheld by the
403 Ankang reservoir during June–October and released later in the year. This operational pattern is
404 well captured by the LSTM+Reservoir model driven by observed meteorological forcings,
405 yielding *NSE* values of 0.91 and 0.89 for the calibration and validation periods, respectively. While
406 slightly lower than those for inflow, these values reflect satisfactory performance given the
407 complexity of human-influenced reservoir operations.

408 Figures 5(a) and 5(c) also show the ensemble-averaged hydrographs from the
409 ISIMIP3b_ref/LSTM and ISIMIP3b_ref/LSTM+Reservoir experiments, driven by ISIMIP3b
410 meteorological forcings rather than historical meteorological observations. The model
411 performance under these forcings is noticeably weaker than that of the OBS/LSTM and
412 OBS/LSTM+Reservoir configurations, likely due to limitations of ISIMIP3b in characterizing
413 regional-scale meteorological regimes (Kang et al., 2023). FDCs in Figure 5(b) and 5(d) further
414 indicate that simulated low flows tend to be overestimated at high exceedance probabilities, which
415 may affect the absolute magnitude of simulated low-flow conditions. Nevertheless, because
416 subsequent analyses focus on changes relative to the ISIMIP3b_ref baseline, the influence of this
417 systematic bias is likely to be attenuated. These simulations are therefore used for the subsequent
418 hydrological drought analysis.



419

420

421 **Figure 5.** Evaluation of monthly reservoir inflow and release simulations. (a, c) Hydrographs of
 422 reservoir inflow and release; (b, d) Corresponding flow duration curves (FDCs). Simulations
 423 driven by meteorological observations (OBS/LSTM and OBS/LSTM+Reservoir) are marked as
 424 blue lines, while simulations driven by ISIMIP3b_ref forcings (ISIMIP3b_ref/LSTM and
 425 ISIMIP3b_ref/LSTM+Reservoir) are marked as orange lines. Shaded bands in (a, c) indicate the
 426 ensemble mean ± 1 standard deviation of simulations driven by ISIMIP3b GCM forcings, while
 427 those in (b, d) denote the interannual range (min–max envelope) of annual FDCs.

428

429

430

431

432

433

Changes in reservoir storage (ΔS) represent another key variable in our operation simulations

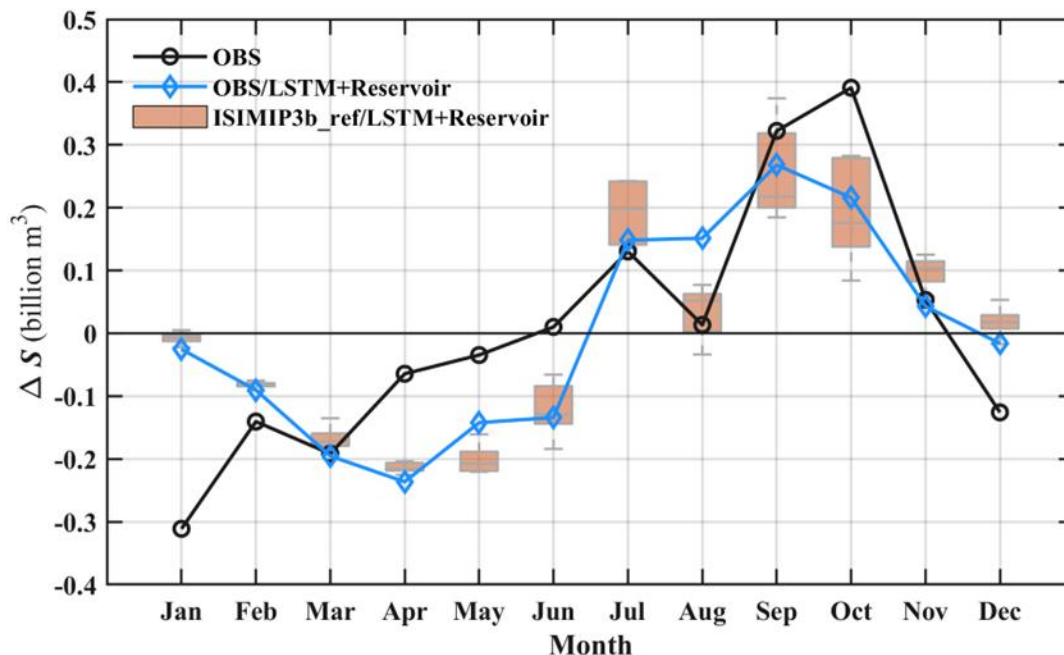
and are also used in the hydropower performance assessment in Section 4.4. Figure 6 illustrates

the observed and simulated mean monthly storage variations over the available period 2001–2010.

Both the OBS/LSTM+Reservoir and ISIMIP3b_ref/LSTM+Reservoir simulations reproduce the

observed dynamics well, particularly the storage accumulation from July to November. With

434 correlation coefficients between simulated and observed storage series ranging from 0.70 to 0.73,
 435 the model provides a reasonable approximation of reservoir operations.



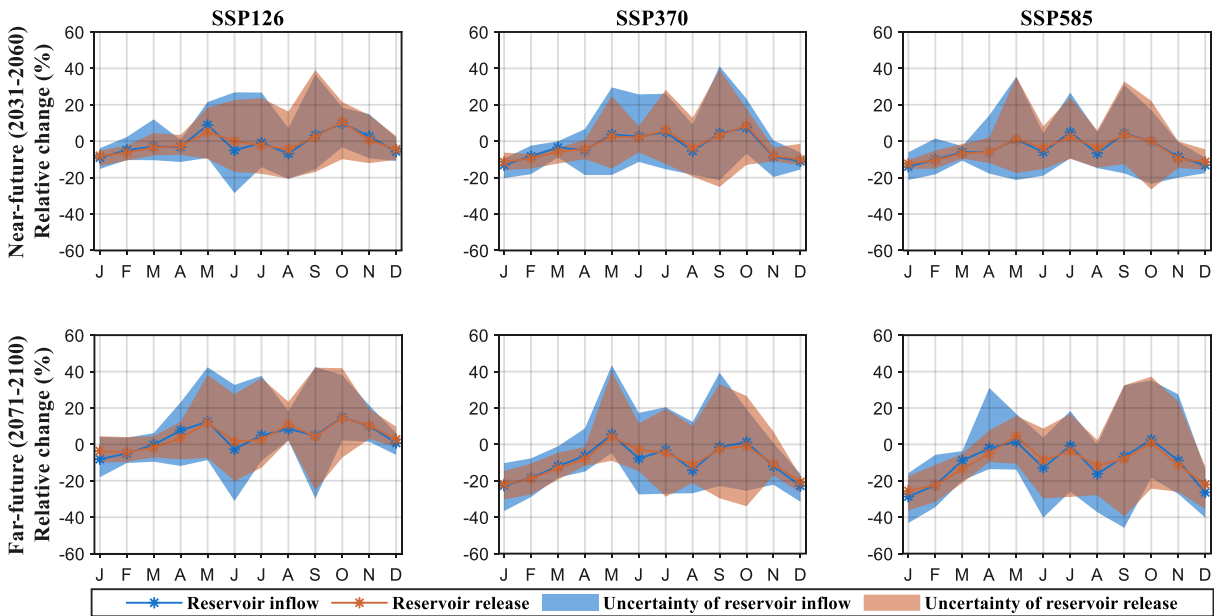
436
 437 **Figure 6.** mean monthly storage variations (ΔS) in the Ankang reservoir during 2001-2010. The
 438 black dotted line represents the multi-year observations. The blue line shows the
 439 OBS/LSTM+Reservoir simulation. The orange boxplots represent the
 440 ISIMIP3b_ref/LSTM+Reservoir ensemble simulations driven by five ISIMIP3b GCMs.

441
 442 4.2 Streamflow variation under the impacts of climate change and reservoir operation

443 ISIMIP3b climate projections indicate a consistent upward trend in both precipitation and
 444 temperature over the UHRB during future periods relative to the reference period (at a significance
 445 level of $p < 0.05$ based on the Mann-Kendall test). Among the SSP scenarios, SSP126 presents an
 446 increase in precipitation (+7.3% to +13.3%) and a modest temperature rise (+1.7°C to +1.9°C).
 447 SSP370 shows a similar increase in precipitation (+7.3% to +11.2%) but a more pronounced
 448 warming (+1.8°C to +4.0°C). Under SSP585, the largest increases are projected for both
 449 precipitation (+8.0% to +15.8%) and temperature (+2.3°C to +5.3°C). As a result of the combined
 450 climatic drivers, the multi-year average reservoir inflow is expected to increase from +0.3% (near-

451 future, 2031–2060) to +5.5% (far-future, 2071–2100) under SSP126. Under SSP370 and SSP585,
452 it is expected to shift from +0.2% (near-future) to –7.0% (far-future), and from –2.6% (near-future)
453 to –8.4% (far-future), respectively, suggesting a potential long-term decline despite short-term
454 gains. This implies that warming-induced evaporation losses may outweigh the compensating
455 effects of increased precipitation, especially under higher-emission scenarios (Satoh et al., 2022).

456 Figure 7 further illustrates the projected relative change in monthly mean streamflow
457 across future periods and SSP scenarios, explicitly highlighting the seasonal influence of both
458 climate change and reservoir operation. Substantial inter-model uncertainty is evident, particularly
459 under SSP585 during the far-future flood season, where streamflow changes range from –45% to
460 +43%. Despite this variability, the ensemble mean reveals a consistent signal: positive deviations
461 are mainly concentrated in the flood season, while most other months are expected to experience
462 declining streamflow. This asymmetric seasonal response suggests an intensification of
463 hydrological seasonality, with wetter periods becoming more flood-prone and drier periods
464 experiencing heightened water stress. In general, human-regulated reservoir operation has the
465 potential to moderate the magnitude of future monthly streamflow changes. However, across all
466 scenarios, the extent to which the Ankang Reservoir alters streamflow patterns remains rather
467 limited, which may be attributable to its primary operational objective of hydropower generation,
468 with relatively little emphasis on shaping the flow regime itself. Further investigation into effective
469 reservoir management is warranted.



470

471 **Figure 7.** Relative changes in projected monthly reservoir inflow and release for two future periods
 472 and three SSP scenarios, relative to the reference period 1985–2014. Lines are the ensemble mean
 473 of the five GCMs, and shaded areas represent the uncertainty across the five GCMs.

474

475 **4.3 Changes in hydrological drought events**

476

477

478

479

480

481

482

483

484

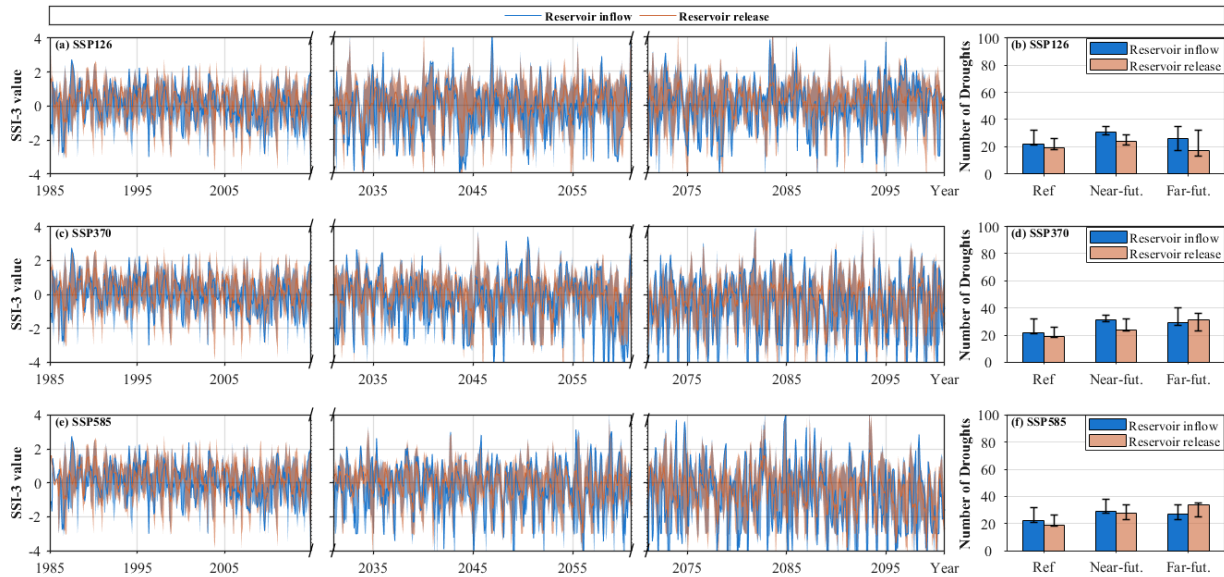
485

486

To comprehensively evaluate future hydrological droughts, we analyzed both the continuous SSI-based drought characteristics and the annual drought event frequency and severity under different climate and reservoir operation scenarios. The time series of SSI-3 associated with reservoir inflow and release, together with their ensemble spreads under three emission scenarios, are shown in Figure 8, with the SSI-1 and SSI-12 results provided in Figures S1 and S2, respectively. SSI-1 and SSI-3 exhibit stronger short-term fluctuations within $[-3, 3]$, whereas SSI-12 shows smoother variability, reflecting more stable long-term dynamics. Consistent with the projected decreases in streamflow, all three indices (SSI-1, SSI-3, and SSI-12) show a slight worsening trend over time, particularly under SSP370 and SSP585, indicating an increased likelihood of drought occurrence in the future (Figures 8(b), 8(d) and 8(f)). We therefore quantified the number of drought events for three periods estimated by the GCMs and summarized them on

487 the right side of Figures 8, S1 and S2. Drought occurrence is generally higher in the future periods
488 than in the reference period, despite substantial inter-model discrepancies across GCMs. The near-
489 future period shows slightly more drought events than the far-future period, with more small and
490 frequent droughts. In addition, as shown in Figure 8 (b), (d), and (f), reservoir operation can
491 mitigate the frequency of drought in the reference period but does not completely remove the risk
492 of hydrological drought under future climate change. Reservoir operation is better at preventing
493 short-term droughts, as the drop in the number of droughts associated with reservoir release versus
494 inflow is significant for SSI-1 in Figure S1 but not for SSI-12 in Figure S2. It may be related to
495 the limited annual regulation capacity of the Ankang reservoir.

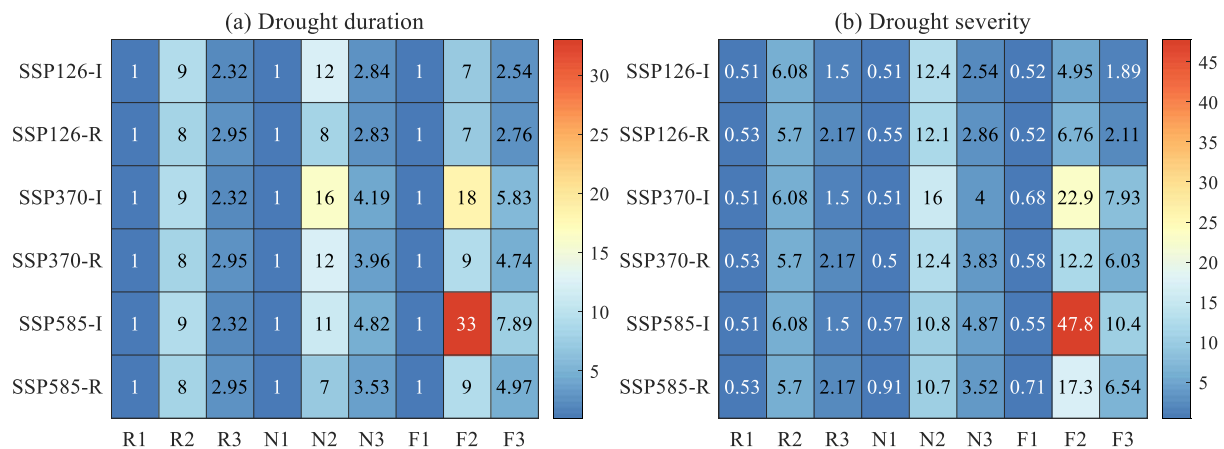
496 A more comprehensive assessment of SSI-3 drought characteristics, including duration and
497 severity, is provided in Figure 9 (see Figure S3 and Figure S4 for SSI-1 and SSI-12, respectively).
498 Both drought duration and severity are projected to deteriorate under future climate change. The
499 most extreme SSI-3 drought event is projected to occur in the far-future period under SSP585,
500 with a maximum duration of 33 months and a maximum severity of 47.8. It is followed by SSP370,
501 with an 18-month duration and a severity of 22.9, and finally SSP126, with a 12-month duration
502 and a severity of 12.4. The drought duration and severity associated with SSI-1 and SSI-12 show
503 a similar pattern. Overall, SSP585 exerts the most pronounced impact on hydrological drought in
504 the region. Notably, reservoir operation substantially alleviates extreme hydrological drought by
505 redistributing streamflow deficits through impoundment and release regulation. For the far-future
506 period under SSP585, the maximum duration associated with SSI-3 is reduced by 72.73% and the
507 maximum severity is reduced by 63.81% due to reservoir operation. A similar moderating effect
508 is observed for SSI-1 (Figure S3), yet the effect is less evident for SSI-12, suggesting that
509 additional human interventions may be needed to mitigate long-term droughts.



510

511 **Figure 8.** Hydrological drought SSI-3 for reference and future periods over the UHRB. (a) Time
 512 series of SSI-3 associated with reservoir inflow and release for the low-emission SSP126 scenario.
 513 Blue and orange intervals indicate their uncertainties, respectively. (b) Number of drought events
 514 for the reference period (1985–2014), near-future period (2031–2060), and far-future period
 515 (2071–2100). Colored bars are ensemble means and error bars represent the estimated difference
 516 in the number of drought events among the five GCMs. (c-d) is the same as (a-b), but for the
 517 medium-emission SSP370 scenario. (e-f) is the same as (a-b), but for the high-emission SSP585
 518 scenario.

519



520

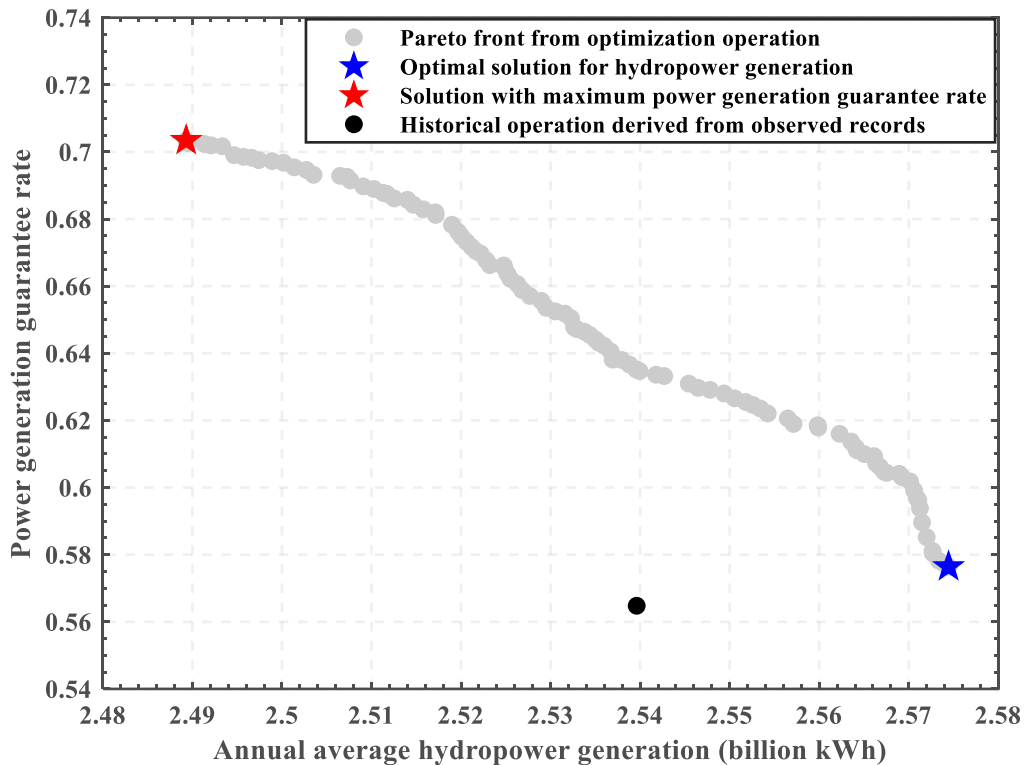
521 **Figure 9.** Heat map representation of (a) drought duration and (b) drought severity for the GCM-
 522 averaged SSI-3 series. The symbols R1, R2 and R3 indicate the minimum, maximum, and mean
 523 values during the reference period (1985–2014). N1, N2 and N3 are the same, but for the near-
 524 future period (2031–2060). F1, F2, and F3 are for the far-future period (2071–2100). Additionally,
 525 SSP126-I and SSP126-R are associated with reservoir inflow and release in the SSP126 scenario,

526 SSP370-I and SSP370-R with the SSP370 scenario, and SSP585-I and SSP585-R with the SSP585
527 scenario.

528

529 4.4 Adaptability of optimal operating policies to future hydrological droughts

530 Optimal reservoir operating policies can serve as a potential adaptation measure to future
531 climate change. Previous studies have highlighted their potential in mitigating the adverse impacts
532 of severe hydrological events (Wu et al., 2023; Sun et al., 2023; Yun et al., 2021b; Levey and
533 Sankarasubramanian, 2025). However, their practical validation remains limited. In this section,
534 we applied the NSGA-II algorithm to derive 100 Pareto-optimal operating policies using historical
535 inflow observations (Figure 10), and examined their implications for future hydropower generation
536 and drought characteristics under climate change.

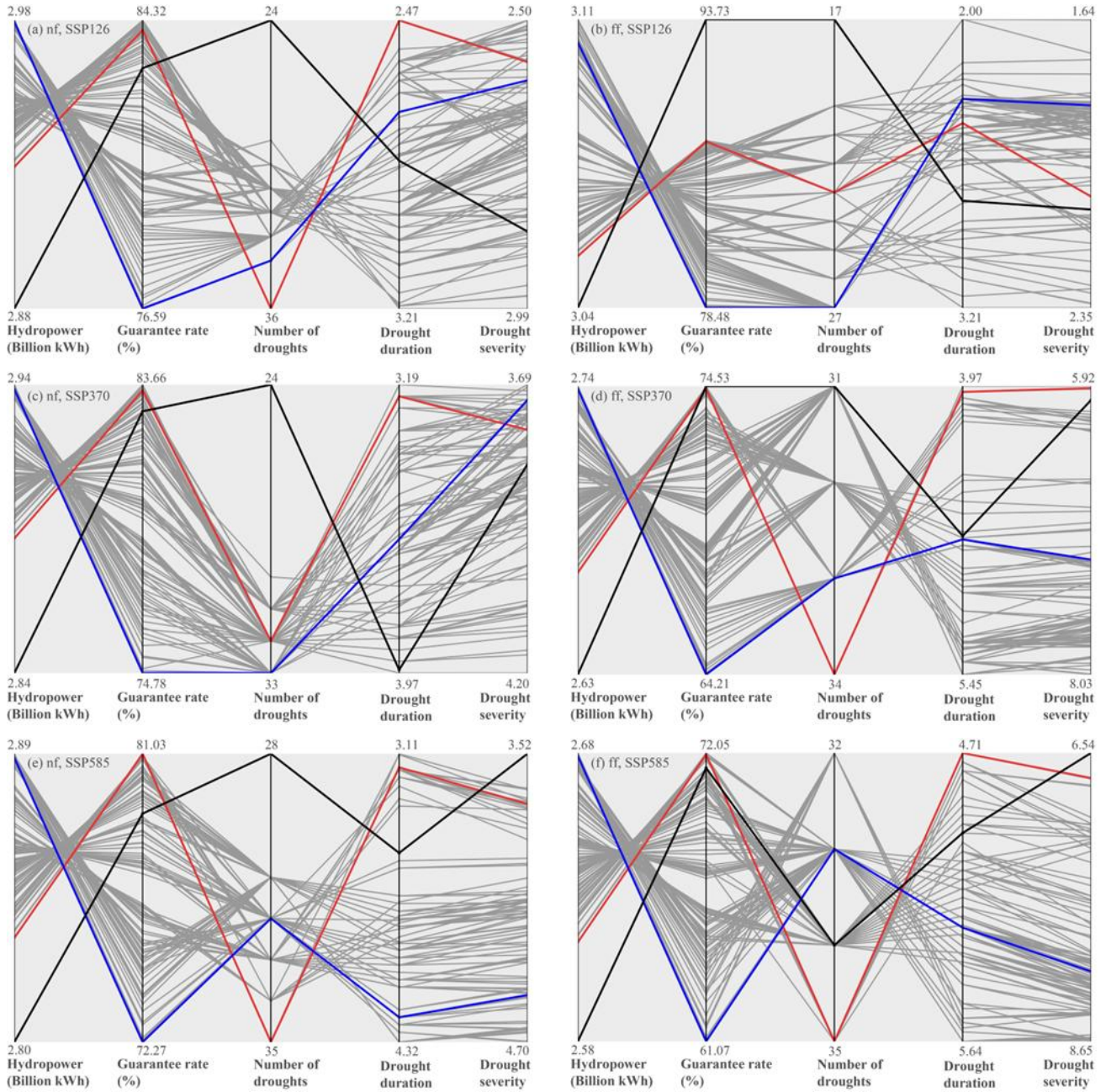


537

538 **Figure 10.** Trade-off between annual average hydropower generation and power generation
539 guarantee rate for the Ankang Reservoir. Each grey dot represents an optimal operating policy
540 identified using the NSGA-II algorithm, forming the Pareto front. The blue star marks the solution
541 with the maximum hydropower generation, while the red star indicates the solution with the

542 highest power generation guarantee rate. The black dot represents the historical operation derived
543 from observed records.
544

545 The simulation results of these 100 optimal operating policies for hydropower generation
546 and SSI-3 drought characteristics under future climate change conditions are reported in Figure 11
547 using parallel coordinate plots. The historically derived operating policy is outlined in black for
548 comparison. These plots show each operating policy as a grey line that intersects each vertical axis
549 at the achievable performance value, and the axes are oriented with the optimal direction upwards.
550 The ideal policy in Figure 11 is, therefore, a horizontal line across the top of each axis.
551 Nevertheless, these lines usually intersect between adjacent axes because superior performance in
552 one indicator comes at the cost of poorer performance in another. For instance, lower power
553 generation guarantee rates inevitably constrain the goal of maximizing annual average hydropower
554 generation. All optimal policies have similar future annual average hydropower generation, except
555 for the far-future period under SSP126. They have a wide range of guarantee rates, such as
556 76.59%–84.32% for the near-future period under SSP126 and 61.07%–72.05% for the far-future
557 period under SSP585. Additionally, as can be seen in all subplots of Figure 11, all the optimal
558 operating policies result in higher hydropower generation but also a higher drought frequency than
559 the historically derived policy. The SSI-3 series associated with optimal reservoir release is broken
560 into more drought events where the average duration and severity of droughts do not change
561 substantially. The most challenging drought management task remains in the future-period under
562 SSP585, during which the historically derived policy has the lowest drought severity. Overall, only
563 a small number of optimal policies achieve robust and satisfactory performance of all considered
564 indicators across plausible future scenarios, demonstrating their potential for mitigating short-term
565 hydrological droughts.



566 **Figure 11.** Trade-offs among hydropower generation, guarantee rate, and SSI-3 drought
567 characteristics under optimal and historical reservoir operating policies using parallel coordinates
568 plots. Panels (a–b) correspond to the near-future (nf) and far-future (ff) under SSP126, (c–d) under
569 SSP370, and (e–f) under SSP585. The grey lines represent Pareto-optimal policies, while the red
570 and blue lines indicate the solutions with the highest guarantee rate and maximum hydropower
571 generation, respectively, and the black line indicates the historical operating pattern. Each axis
572 represents an objective, with the optimal direction oriented upwards.

573

574 4.5 Limitations, uncertainties, and implications

575 While the proposed framework provides a data-driven way to represent reservoir-regulated
576 hydrological droughts under future climate scenarios, several limitations and sources of
577 uncertainty should be explicitly acknowledged. These aspects are important for interpreting the
578 robustness, scope, and broader applicability of our results.

579 **I) Possible non-stationarity of the operating environment and limited climate-model**
580 **sampling.** In our framework, the physics-guided LSTM module learns reservoir operating
581 behavior from historical conditions and is subsequently applied to the reference and future periods.
582 This implicitly assumes that the governing operating objectives and constraints remain broadly
583 stable, and that the learned decision logic is transferable across time. Our previous analyses
584 indicate that, for the case investigated here, the reservoir-regulated hydrological response exhibits
585 relatively stable patterns over multi-decadal timescales, supporting the feasibility of using a
586 surrogate model to represent the whole-period operational behavior (He et al., 2023). However,
587 such consistency is case-specific and may not hold in other basins where human interventions are
588 stronger; caution is warranted when applying the proposed approach beyond the study basin. In
589 addition, future projections are driven by a limited set of climate forcings (five ISIMIP3b GCMs),
590 which may not fully span plausible hydroclimatic trajectories and extremes, thereby constraining
591 the uncertainty range of the simulated drought responses. Key extensions include stress-testing
592 surrogate transferability under plausible operational changes and quantifying climate-forcing
593 uncertainty using a larger GCM ensemble.

594 **II) Sensitivity of drought inferences to calibration choices and single-basin LSTM**
595 **training.** Simulated hydrological drought characteristics can depend on the objective function
596 adopted during model calibration (Knoben et al., 2019). In this study, calibration primarily relied

597 on *NSE*, which tends to emphasize high-flow conditions at the expense of low-flow fidelity. This
598 may affect drought assessments because, at the low-flow end of the flow regime (i.e., high
599 exceedance probabilities), streamflow deficits play a dominant role in shaping drought onset,
600 persistence, and severity. Consistent with this concern, the FDCs in Figures 5(b) and 5(d) indicate
601 a systematic high bias in low flows, implying that the absolute magnitude of drought intensity
602 derived from simulated streamflow may be underestimated. Although our subsequent analyses
603 focus on relative changes with respect to the ISIMIP3b_ref baseline, this sensitivity should be
604 acknowledged. A more drought-facing calibration setup, e.g., low-flow-oriented objectives (log-
605 transformed *NSE*), provides a direct path to reduce this sensitivity.

606 Beyond calibration, the physics-guided LSTM surrogate in our framework is trained using
607 data from a single reservoir-regulated basin, which constrains the training envelope to the
608 historical range of hydroclimatic and operational conditions represented in that system. This design
609 choice was primarily motivated by limited access to harmonized reservoir operation records across
610 regulated basins and by our focus on the target reservoir-regulated basin. Recent guidance for
611 rainfall–runoff LSTM modeling highlights that single-basin training can limit generalization,
612 particularly for extreme events, whereas multi-basin training on hydrologically diverse data is
613 often more robust (Kratzert et al., 2024). As data availability permits, a natural extension is to
614 conduct multi-basin (or multi-reservoir-system) training followed by fine-tuning to the target basin,
615 and to explicitly evaluate how such training affects the simulation of drought-relevant low flows
616 and extreme drought events.

617 **III) Limitations in the design of our optimized operating policy.** Many reservoir
618 optimization studies remain at a preliminary stage, where operating rules are optimized using
619 historical observations and then deemed superior based solely on comparisons with historical

620 performance. Although the observed historical operation, which is shaped by complex real-world
621 objectives and constraints, is Pareto-dominated in the objective space of annual average
622 hydropower generation and power-generation guarantee rate (Figure 10), it is not necessarily
623 outperformed by most Pareto-optimal policies under future scenarios, particularly in terms of
624 guarantee rate and drought frequency (Figure 11). In addition, a common challenge with Pareto-
625 optimal solution sets is selecting a single implementable policy. By benchmarking the future
626 performance of candidate Pareto solutions against the historical operating policy, we found that
627 the reliability-oriented solution, that is, the one with the highest guarantee rate, performs better
628 than the historical operating policy across most future scenarios, except for drought frequency,
629 whereas the hydropower-optimal solution does not show consistent advantages. Hydropower
630 generation is broadly similar across the Pareto set in future periods, suggesting limited
631 differentiation in this metric. These findings together suggest that for the Ankang system, the
632 reliability-oriented solution is a more defensible candidate for implementation. Additionally, the
633 optimized policies in our drought-focused analysis were derived primarily for hydropower
634 generation and power generation guarantee rate and were then directly applied to future scenarios
635 to examine trade-offs with hydrological drought mitigation. This indicates scope for further
636 improvements in drought mitigation performance. Future work could incorporate drought-event
637 characteristics as explicit objectives or constraints, and consider other human interventions (e.g.,
638 inter-basin water transfers and urbanization) to better bracket plausible drought-mitigation
639 pathways under changing conditions (Wu et al., 2023; Firoz et al., 2018).

640

641 5 Conclusions

642 By coupling an LSTM-based reservoir inflow model with a physics-guided reservoir
643 operation model, this study developed a fully automated ML-based framework to project river
644 streamflow changes over the UHRB under different future scenarios and the associated
645 hydrological droughts. The effects of climate change and reservoir operation were considered
646 sequentially to reveal their different roles. Additionally, the trade-off between future hydrological
647 droughts and operating benefits (i.e., hydropower generation and power generation guarantee rate)
648 was investigated by optimizing the reservoir operating policies. The main findings are summarized
649 as follows:

650 1. A reasonable LSTM-based model architecture is recommended for hydrological
651 simulation in the reservoir-regulated region. When ISIMIP3b historical meteorological forcing is
652 used instead of observed meteorological forcing, the model can still reproduce the inflow and
653 release of the Ankang Reservoir, as well as changes in reservoir storage. This demonstrates the
654 feasibility of projecting future streamflow and associated hydrological droughts using ML
655 approaches.

656 2. Future climate change over the UHRB tends to reduce natural streamflow and exacerbate
657 hydrological droughts, especially in the far-future period (2071-2100) under the SSP585 scenario.
658 While the operation of the Ankang Reservoir can mitigate the frequency, duration, and severity of
659 short-term hydrological droughts (SSI-1 and SSI-3), it shows limited effectiveness in alleviating
660 long-term droughts (SSI-12).

661 3. The optimal reservoir operating policies at Ankang Reservoir, designed to maximize
662 hydropower generation and power generation guarantee rates, highlight clear trade-offs between
663 hydrological drought risk and hydropower benefits, especially in the near-future period (2031-

664 2060). Compared to the historically derived policy, these optimal strategies yield higher
665 hydropower benefits but may also lead to increased drought frequency. The finding that a small
666 subset of optimal policies consistently delivers robust performance across multiple indicators
667 under plausible future scenarios underscores the potential of these policies to enhance regional
668 water resources management under climate change.

669

670 **Declaration of Competing Interest**

671 The authors declare that they have no known competing financial interests or personal
672 relationships that could have appeared to influence the work reported in this paper.

673

674 **Data availability**

675 The code that supports the findings of this study is available from the corresponding author
676 upon reasonable request. The ISIMIP3b data used in producing this paper are available at
677 <https://data.isimip.org/search/tree/ISIMIP3b/InputData/>. Observed streamflow data are available
678 from the Bureau of Hydrology of the Yangtze Water Resources Commission of China
679 (<https://www.cjh.com.cn>).

680

681 **Author contribution**

682 YG, KC and SH designed the study. SH, SS, and YL developed the models, with SH and LZ
683 implementing them. SH drafted the manuscript in close collaboration with YG, SS, YL contributed
684 to the data curation. Throughout the study period, all the authors engaged in discussions regarding
685 the results, provided critical feedback, and approved the final version of the paper.

686

687 **Supplement**

688 The supplement related to this article is available at.

689

690 **Financial support**

691 This research has been supported by the National Key Research and Development Program
692 of China (2023YFC3209502), National Natural Science Foundation of China (U2340217,
693 42577102 and 52595704), and the Basic Research Program of Jiangsu (BK20250013).

694 **References**

- 695 Abadi, M., Barham, P., Chen, J., Chen, Z., and Davis, A.: TensorFlow: a system for large-scale machine learning In:
696 Proceedings of the 12th USENIX conference on Operating Systems Design and Implementation. USENIX
697 Association, Savannah, GA, USA, 265-283, 2016.
- 698 Arsenault, R., Martel, J.-L., Brunet, F., Brissette, F., and Mai, J.: Continuous streamflow prediction in ungauged
699 basins: long short-term memory neural networks clearly outperform traditional hydrological models, *Hydrol Earth*
700 *Syst Sc*, 27, 139-157, 10.5194/hess-27-139-2023, 2023.
- 701 Bertoni, F., Castelletti, A., Giuliani, M., and Reed, P. M.: Discovering Dependencies, Trade-Offs, and Robustness in
702 Joint Dam Design and Operation: An Ex-Post Assessment of the Kariba Dam, *Earth's Future*, 7, 1367-1390,
703 10.1029/2019ef001235, 2019.
- 704 Brunner, M. I.: Reservoir regulation affects droughts and floods at local and regional scales, *Environ Res Lett*, 16,
705 124016, 10.1088/1748-9326/ac36f6, 2021.
- 706 Chai, Y., Yue, Y., Slater, L. J., Yin, J., Borthwick, A. G. L., Chen, T., and Wang, G.: Constrained CMIP6
707 projections indicate less warming and a slower increase in water availability across Asia, *Nat Commun*, 13, 4124,
708 10.1038/s41467-022-31782-7, 2022.
- 709 Chang, L., Cheng, L., Zhang, L., Han, D., Zhang, J., and Liu, P.: Remote sensing-based high-resolution reservoir
710 drought index for identifying the occurrence and propagation of hydrological droughts in a large river basin, *Remote*
711 *Sensing of Environment*, 328, 114859, 10.1016/j.rse.2025.114859, 2025.
- 712 Chen, E. and Yu, X.: A transferable machine learning model for real-time forecast of epidemic dynamics and pre-
713 trigger event warning, *AI in Civil Engineering*, 4, 18, 10.1007/s43503-025-00059-5, 2025.
- 714 Cheng, H., Wang, T., and Yang, D.: Quantifying the Regulation Capacity of the Three Gorges Reservoir on Extreme
715 Hydrological Events and Its Impact on Flow Regime in a Changing Climate, *Water Resour Res*, 60,
716 e2023WR036329, 10.1029/2023wr036329, 2024.
- 717 Cui, Z., Zhou, Y., Guo, S., Wang, J., and Xu, C.-Y.: Effective improvement of multi-step-ahead flood forecasting
718 accuracy through encoder-decoder with an exogenous input structure, *J Hydrol*, 609, 127764,
719 10.1016/j.jhydrol.2022.127764, 2022.
- 720 Culley, S., Noble, S., Yates, A., Timbs, M., Westra, S., Maier, H. R., Giuliani, M., and Castelletti, A.: A bottom-up
721 approach to identifying the maximum operational adaptive capacity of water resource systems to a changing climate,
722 *Water Resour Res*, 52, 6751-6768, 10.1002/2015wr018253, 2016.
- 723 Dams, C. N. C. o. L.: Ankang hydropower project. Beijing: Chinese National Committee on Large Dams (in
724 Chinese), 2011.
- 725 Deb, K., Pratap, A., Agarwal, S., and Meyarivan, T.: A fast and elitist multiobjective genetic algorithm: NSGA-II,
726 *Ieee T Evolut Comput*, 6, 182-197, 10.1109/4235.996017, 2002.
- 727 Eriyagama, N., Smakhtin, V., and Udamura, L.: How much artificial surface storage is acceptable in a river basin
728 and where should it be located: A review, *Earth-Science Reviews*, 208, 103294, 10.1016/j.earscirev.2020.103294,
729 2020.

730 Firoz, A. B. M., Nauditt, A., Fink, M., and Ribbe, L.: Quantifying human impacts on hydrological drought using a
731 combined modelling approach in a tropical river basin in central Vietnam, *Hydrol Earth Syst Sc*, 22, 547-565,
732 10.5194/hess-22-547-2018, 2018.

733 G. Ribeiro Neto, G., Kchouk, S., Melsen, L. A., Cavalcante, L., Walker, D. W., Dewulf, A., Costa, A. C., Martins,
734 E. S. P. R., and van Oel, P. R.: HESS Opinions: Drought impacts as failed prospects, *Hydrol Earth Syst Sc*, 27,
735 4217-4225, 10.5194/hess-27-4217-2023, 2023.

736 García-Feal, O., González-Cao, J., Fernández-Nóvoa, D., Astray Dopazo, G., and Gómez-Gesteira, M.: Comparison
737 of machine learning techniques for reservoir outflow forecasting, *Natural Hazards and Earth System Sciences*, 22,
738 3859-3874, 10.5194/nhess-22-3859-2022, 2022.

739 Gu, L., Chen, J., Yin, J., Xu, C. Y., and Zhou, J.: Responses of precipitation and runoff to climate warming and
740 implications for future drought changes in China, *Earth's Future*, 8, e2020EF001718, 10.1029/2020ef001718, 2020.

741 Gudmundsson, L., Boulange, J., Do, H. X., Gosling, S. N., Grillakis, M. G., Koutroulis, A. G., Leonard, M., Liu, J.,
742 Müller Schmied, H., Papadimitriou, L., Pokhrel, Y., Seneviratne, S. I., Satoh, Y., Thiery, W., Westra, S., Zhang, X.,
743 and Zhao, F.: Globally observed trends in mean and extreme river flow attributed to climate change, *Science*, 371,
744 1159-1162, 10.1126/science.aba3996, 2021.

745 Hanasaki, N., Kanae, S., and Oki, T.: A reservoir operation scheme for global river routing models, *J Hydrol*, 327,
746 22-41, 10.1016/j.jhydrol.2005.11.011, 2006.

747 He, S., Chen, K., Liu, Z., and Deng, L.: Exploring the impacts of climate change and human activities on future
748 runoff variations at the seasonal scale, *J Hydrol*, 619, 129382, 10.1016/j.jhydrol.2023.129382, 2023.

749 He, S., Li, B., Li, Q., Zheng, H., and Chen, Y.: Refining hydropower operation by dynamic control of cascade
750 reservoir water levels with flood season segmentation, *Energy*, 314, 134156, 10.1016/j.energy.2024.134156, 2025.

751 He, S., Guo, S., Zhang, J., Liu, Z., Cui, Z., Zhang, Y., and Zheng, Y.: Multi-objective operation of cascade
752 reservoirs based on short-term ensemble streamflow prediction, *J Hydrol*, 610, 127936,
753 10.1016/j.jhydrol.2022.127936, 2022.

754 Ho, S. Q.-G. and Ehret, U.: Is drought protection possible without compromising flood protection? Estimating the
755 potential dual-use benefit of small flood reservoirs in southern Germany, *Hydrol Earth Syst Sc*, 29, 2785-2810,
756 10.5194/hess-29-2785-2025, 2025.

757 Hochreiter, S.: The Vanishing Gradient Problem During Learning Recurrent Neural Nets and Problem Solutions,
758 *International Journal of Uncertainty, Fuzziness and Knowledge-Based Systems*, 06, 107-116,
759 10.1142/s0218488598000094, 1998.

760 Hochreiter, S. and Schmidhuber, J.: Long short-term memory, *Neural Computation*, 9, 1735-1780,
761 10.1162/neco.1997.9.8.1735, 1997.

762 Hosking, J. R. M.: L-Moments: Analysis and estimation of distributions using linear combinations of order statistics,
763 *Journal of the Royal Statistical Society: Series B (Methodological)*, 52, 105-124, 10.1111/j.2517-
764 6161.1990.tb01775.x, 1990.

765 Huang, J., Wu, W., Maier, H. R., Hughes, J., Wang, Q. J., and Cao, Y.: Comprehensive framework for long-term
766 reservoir management under deep uncertainty, *Environ Modell Softw*, 195, 106740, 10.1016/j.envsoft.2025.106740,
767 2026.

768 Huang, J., Sangiorgio, M., Wu, W., Maier, H. R., Wang, Q. J., Hughes, J., and Castelletti, A.: Solving the robustness
769 puzzle: The joint impact of optimization approach, robustness metrics, and scenarios on water resources
770 management under deep uncertainty, *Journal of Environmental Management*, 373, 123540,
771 10.1016/j.jenvman.2024.123540, 2025.

772 IPCC: The Physical Science Basis. Contribution of Working Group I to the Sixth Assessment Report of the
773 Intergovernmental Panel on Climate Change. Cambridge University Press, 2021.

774 Ji, P., Yuan, X., and Jiao, Y.: Future hydrological drought changes over the upper Yellow River basin: The role of
775 climate change, land cover change and reservoir operation, *J Hydrol*, 617, 129128, 10.1016/j.jhydrol.2023.129128,
776 2023.

777 Jin, H., Willems, P., Chen, X., and Liu, M.: Nonstationary flood and its influencing factors analysis in the Hanjiang
778 River Basin, China, *J Hydrol*, 625, 129994, 10.1016/j.jhydrol.2023.129994, 2023.

779 Kang, S., Yin, J., Gu, L., Yang, Y., Liu, D., and Slater, L.: Observation-constrained projection of flood risks and
780 socioeconomic exposure in China, *Earth's Future*, 11, e2022EF003308, 10.1029/2022ef003308, 2023.

781 Kheyri, Y., Sharafati, A., and Neshat, A.: The socioeconomic impact of severe droughts on agricultural lands over
782 different provinces of Iran, *Agricultural Water Management*, 289, 108550, 10.1016/j.agwat.2023.108550, 2023.

783 Kingma, D. P. and Ba, J.: Adam: a method for stochastic optimization. arXiv:1412.6980 [cs.LG]. 2014.

784 Knoben, W. J. M., Freer, J. E., and Woods, R. A.: Technical note: Inherent benchmark or not? Comparing Nash–
785 Sutcliffe and Kling–Gupta efficiency scores, *Hydrol Earth Syst Sc*, 23, 4323–4331, 10.5194/hess-23-4323-2019,
786 2019.

787 Kratzert, F., Gauch, M., Klotz, D., and Nearing, G.: HESS Opinions: Never train a Long Short-Term Memory
788 (LSTM) network on a single basin, *Hydrol Earth Syst Sc*, 28, 4187–4201, 10.5194/hess-28-4187-2024, 2024.

789 Lange, S.: Trend-preserving bias adjustment and statistical downscaling with ISIMIP3BASD (v1.0), *Geosci. Model*
790 *Dev.*, 12, 3055–3070, 10.5194/gmd-12-3055-2019, 2019.

791 Levey, J. R. and Sankarasubramanian, A.: Is Reservoir Storage Effectively Utilized in the Southeastern US? A
792 Regional Assessment to Improve Water Supply Availability Considering Potential Storage and Flood Scenarios,
793 *Earth's Future*, 13, e2024EF005176, 10.1029/2024ef005176, 2025.

794 Liu, J., Yuan, X., Zeng, J., Jiao, Y., Li, Y., Zhong, L., and Yao, L.: Ensemble streamflow forecasting over a cascade
795 reservoir catchment with integrated hydrometeorological modeling and machine learning, *Hydrol Earth Syst Sc*, 26,
796 265–278, 10.5194/hess-26-265-2022, 2022.

797 Longyang, Q. and Zeng, R.: A Hierarchical Temporal Scale Framework for Data-Driven Reservoir Release
798 Modeling, *Water Resour Res*, 59, e2022WR033922, 10.1029/2022wr033922, 2023.

799 Özdoğan-Sarıkoç, G., Sarıkoç, M., Celik, M., and Dadaser-Celik, F.: Reservoir volume forecasting using artificial
800 intelligence-based models: Artificial Neural Networks, Support Vector Regression, and Long Short-Term Memory,
801 *J Hydrol*, 616, 128766, 10.1016/j.jhydrol.2022.128766, 2023.

802 Quinn, J. D., Reed, P. M., Giuliani, M., and Castelletti, A.: What is controlling our control rules? Opening the black
803 box of multireservoir operating policies using time-varying sensitivity analysis, *Water Resour Res*, 55, 5962–5984,
804 10.1029/2018wr024177, 2019.

805 Rehana, S. and Rajesh, M.: Assessment of impacts of climate change on Indian riverine thermal regimes using
806 hybrid deep learning methods, *Water Resour Res*, 59, e2021WR031347, 10.1029/2021wr031347, 2023.

807 Satoh, Y., Yoshimura, K., Pokhrel, Y., Kim, H., Shioyama, H., Yokohata, T., Hanasaki, N., Wada, Y., Burek, P.,
808 Byers, E., Schmied, H. M., Gerten, D., Ostberg, S., Gosling, S. N., Boulange, J. E. S., and Oki, T.: The timing of
809 unprecedented hydrological drought under climate change, *Nat Commun*, 13, 3287, 10.1038/s41467-022-30729-2,
810 2022.

811 Shukla, S. and Wood, A. W.: Use of a standardized runoff index for characterizing hydrologic drought, *Geophysical*
812 *Research Letters*, 35, L02405, 10.1029/2007gl032487, 2008.

813 Smith, K. A., Barker, L. J., Tanguy, M., Parry, S., Harrigan, S., Legg, T. P., Prudhomme, C., and Hannaford, J.: A
814 multi-objective ensemble approach to hydrological modelling in the UK: an application to historic drought
815 reconstruction, *Hydrol Earth Syst Sc*, 23, 3247–3268, 10.5194/hess-23-3247-2019, 2019.

816 Solanki, H., Vegad, U., Kushwaha, A., and Mishra, V.: Improving Streamflow Prediction Using Multiple
817 Hydrological Models and Machine Learning Methods, *Water Resour Res*, 61, e2024WR038192,
818 10.1029/2024wr038192, 2025.

819 Sun, J., Chen, W., Hu, B., Xu, Y. J., Zhang, G., Wu, Y., Hu, B., and Song, Z.: Roles of reservoirs in regulating basin
820 flood and droughts risks under climate change: Historical assessment and future projection, *Journal of Hydrology:*
821 *Regional Studies*, 48, 101453, 10.1016/j.ejrh.2023.101453, 2023.

822 Tran, H., Zhou, T., Tan, Z., Fang, Y., and Ruby Leung, L.: Improving the prediction of daily reservoir releases over
823 the CONUS using conditioned LSTM, *J Hydrol*, 661, 133750, 10.1016/j.jhydrol.2025.133750, 2025.

824 Vicente-Serrano, S. M., Lopez-Moreno, J. I., Begueria, S., Lorenzo-Lacruz, J., Azorin-Molina, C., and Moran-
825 Tejada, E.: Accurate computation of a streamflow drought index, *Journal of Hydrologic Engineering*, 17, 318–332,
826 10.1061/(Asce)He.1943-5584.0000433, 2012.

827 Wan, W., Wang, Z., Cheng, L., Bai, Y., Wang, W., and Wang, K.: Integrating Drought Warning Water Level With
828 Analytical Hedging for Reservoir Water Supply Operation, *Water Resour Res*, 61, e2024WR038680,
829 10.1029/2024wr038680, 2025.

830 Wan, W., Zhao, J., Li, H. Y., Mishra, A., Hejazi, M., Lu, H., Demissie, Y., and Wang, H.: A holistic view of water
831 management impacts on future Droughts: A Global Multimodel Analysis, *Journal of Geophysical Research:*
832 *Atmospheres*, 123, 5947–5972, 10.1029/2017jd027825, 2018.

833 Wanders, N. and Wada, Y.: Human and climate impacts on the 21st century hydrological drought, *J Hydrol*, 526,
834 208–220, 10.1016/j.jhydrol.2014.10.047, 2015.

835 Wu, G., Chen, J., Shi, X., Kim, J. S., Xia, J., and Zhang, L.: Impacts of global climate warming on meteorological
836 and hydrological droughts and their propagations, *Earth's Future*, 10, e2021EF002542, 10.1029/2021ef002542,
837 2022.

838 Wu, J., Chen, X., Yao, H., Gao, L., Chen, Y., and Liu, M.: Non-linear relationship of hydrological drought
839 responding to meteorological drought and impact of a large reservoir, *J Hydrol*, 551, 495-507,
840 10.1016/j.jhydrol.2017.06.029, 2017.

841 Wu, Y., Sun, J., Hu, B., Xu, Y. J., Rousseau, A. N., and Zhang, G.: Can the combining of wetlands with reservoir
842 operation reduce the risk of future floods and droughts?, *Hydrol Earth Syst Sc*, 27, 2725-2745, 10.5194/hess-27-
843 2725-2023, 2023.

844 Yang, S., Yang, D., Chen, J., and Zhao, B.: Real-time reservoir operation using recurrent neural networks and
845 inflow forecast from a distributed hydrological model, *J Hydrol*, 579, 124229, 10.1016/j.jhydrol.2019.124229, 2019.

846 Yevjevich, V.: An objective approach to definitions and investigation of continental hydrologic droughts, *Hydrology*
847 *Paper23*. Fort Collins, Colorado State U., 1967.

848 Yun, X., Tang, Q., Sun, S., and Wang, J.: Reducing Climate Change Induced Flood at the Cost of Hydropower in
849 the Lancang-Mekong River Basin, *Geophysical Research Letters*, 48, e2021GL094243, 10.1029/2021gl094243,
850 2021a.

851 Yun, X., Tang, Q., Li, J., Lu, H., Zhang, L., and Chen, D.: Can reservoir regulation mitigate future climate change
852 induced hydrological extremes in the Lancang-Mekong River Basin?, *Sci Total Environ*, 785,
853 10.1016/j.scitotenv.2021.147322, 2021b.

854 Zhang, X., Song, Z., Zhou, T., Wang, D., Wang, Y., and Liu, P.: Reservoir operation strategies to mitigate
855 hydrological drought effects along the middle and lower reaches of the Yangtze River, *Journal of Hydrology:*
856 *Regional Studies*, 58, 102204, 10.1016/j.ejrh.2025.102204, 2025.

857 Zheng, Y., Liu, P., Cheng, L., Xie, K., Lou, W., Li, X., Luo, X., Cheng, Q., Han, D., and Zhang, W.: Extracting
858 operation behaviors of cascade reservoirs using physics-guided long-short term memory networks, *Journal of*
859 *Hydrology: Regional Studies*, 40, 101034, 10.1016/j.ejrh.2022.101034, 2022.

860 Zhou, Z., Shi, H., Fu, Q., Ding, Y., Li, T., and Liu, S.: Investigating the propagation from meteorological to
861 hydrological drought by introducing the nonlinear dependence with directed information transfer index, *Water*
862 *Resour Res*, 57, e2021WR030028, 10.1029/2021wr030028, 2021.

863